Geophysical Prospecting

Increasing the Effectiveness of Electrical Resistivity Tomography Using γ11n Configurations

Journal:	*Geophysical Prospecting*
Manuscript ID:	GP-2013-1694.R3
Manuscript Type:	Original Manuscripts
Date Submitted by the Author:	n/a
Complete List of Authors:	Szalai, Sandor; MTA CSFK Geodéziai és Geofizikai Intézet, Geophysical Lemperger, István; MTA CSFK Geodéziai és Geofizikai Intézet, Kis, Árpád; MTA CSFK Geodéziai és Geofizikai Intézet, Metwaly, Mohamed Szokoli, Kitti; MTA CSFK Geodéziai és Geofizikai Intézet, Geophysical
Keyword:	2D resistivity, Geoelectric methods

Increasing the Effectiveness of Electrical Resistivity Tomography Using γ_{11n} Configurations

Szalai, S., Kis, Á., Metwaly, M., Lemperger, I., Szokoli, K.

RCAES HAS, GGI, H-9401 Sopron POB 5, Hungary,

e-mail: szalai@ggki.hu

ABSTRACT

A new array type, the γ_{11n} arrays are introduced in this paper, in which the sequence of the current (C) and potential (P) electrodes is CPCP and the distance between the last two electrodes is *n* times the distance between the first two ones and that of the second and third one. These arrays are called quasi null arrays because they are – according to their array and behaviour – between the traditional and null arrays. It is shown by numerical modelling that in detection of small-effect inhomogeneities these configurations may be more effective than the traditional ones including the optimised Stummer configuration. Certain γ_{11n} configurations – especially the γ_{112}, γ_{113} and γ_{114} – produced better results both in horizontal and vertical resolution investigations. On the basis of the numerical studies, the γ_{11n} configurations seem to be very promising in problems where the anomalies are similar to the numerically investigated ones, that is they can detect and characterise, for example, tunnels, caves, cables, tubes, abandoned riverbeds or discontinuity in a clay layer with greater efficacy than those of the traditional configurations. γ_{11n} measurements need less data than traditional configurations therefore also the time demand of electrical resistivity tomography (ERT) measurements can be shortened by their use.

Keywords: geoelectric configuration, γ_{11n} configurations, depth of detectability, ERT, quasi null arrays

INTRODUCTION

Geoelectric methods form a traditional group of geophysical techniques (Van Nostrand and Cook 1966; Alpin *et al*. 1966; Zhdanov and Keller 1993). In the early times their use was restricted to mineral exploration. Today they are frequently used in numerous field problems (Butler 2005), related to electrical resistivity distribution of the subsurface: hydrogeology (Kirsch 2006), environmental studies (Ward 1990; Knödel *et al*. 2005), engineering (Ward 1990, Szalai *et al*., 2009a), safety purposes (Metwaly *et al*. 2008) and archaeological problems (Clark 1990), etc.

The number of published geoelectric arrays used for geoelectric measurements is more than one hundred (Szalai and Szarka 2008a). It is widely known (mainly from Ward 1990) that each array has some specific advantages and disadvantages. In studying these qualities, the arrays were compared from many different aspects. One of the key parameters, the depth of the investigation value was calculated by Szalai *et al*. (2009b) following the slightly different definitions given by Edwards (1977) and Roy and Apparao (1971) for all arrays. Parameter sensitivity maps, which are crucial in understanding the different arrays, were presented by Szalai and Szarka (2008b,c) for all arrays that ever existed. Ward (1990) evaluated the geoelectric arrays from 14 various aspects. Although the aforementioned investigations aimed at providing a theoretical basis for traditional profiling and sounding techniques, they are also important for electrical resistivity tomography (ERT) measurements because the individual arrays serve as a basis for the ERT measurements.

Since ERT measurements have become the dominant tool in geoelectric research in the past decades, it is of crucial importance to maximize the information available when using them. There are actually significant efforts to find the best possible, so-called optimized configurations (Furman *et al*., 2003; Stummer *et al*. 2004; Wilkinson *et al.*, 2006). The optimised configurations, e.g. the

Stummer configuration (Stummer *et al*. 2004) – in contrast to the classical configuration approach – may contain a series of very different arrays.

Stummer *et al* (2004) did not however include in the optimisation procedure γ-type arrays, and therefore not the γ_{11n} arrays. In the case of these arrays, the electrodes are positioned in an overlapping mode that is the current, and potential electrodes follow each other alternately (see Fig. 1). The large value of the *k* geometrical factor does not, however, inevitably refer to the field applicability of an array as shown by Szalai *et al* (2002) and Szalai *et al* (2004). *k* is namely the function of the homogeneous half-space value which has nothing to do with the potential due to the inhomogeneities which contain information important for us. If the γ_{11n} arrays will prove to be useful, they have to be taken into account in all optimisation processes.

In the last few years several other motivations accumulated to study the γ_{11n} and γm_{11n} configurations which will be discussed in the next section. First of all however the definition of the applied non-conventional arrays is given. The γ_{11n} arrays are presented in Figure 1. A γm_{11n} (mirrored γ_{11n}) array contains a γ_{11n} array and its pair, a γ_{n11} array. These arrays are the same but they are orientated in opposite directions carrying out measurements. The γm_{11n} configuration which consists of γm_{11n} arrays creates two times more dense data set than the γ_{11n} configuration in itself. $\gamma(m)_{11n}$ refers to both the γ_{11n} and γm_{11n} configurations.

MOTIVATIONS TO STUDY THE γ_{11N} AND γm_{11N} CONFIGURATIONS

a.) Furman *et al.* (2003) performed a sensitivity analysis and demonstrated the supremacy of the "partially overlapping arrays", which are also γ-type arrays, that is their electrode sequence is CPCP. Szalai and Szarka (2008b) presented the normalised parameter sensitivity (nPS) maps of many linear arrays. Many of them are reproduced in Figure 2. In the first row, the nPS maps of the Wenner-α (W-α), Wenner-β (W-β), dipole-axial (Dp-ax) four-electrode and the

P-Dp three-electrode arrays are shown in a depth of one tenth of the array length (The array length is the distance of the farthest electrodes which are not in the infinity). In the second row the nPS maps of several characteristic γ_{n11} arrays are presented which are the oppositely orientated versions of the γ_{11n} arrays therefore their nPS map is also the oppositely orientated version of the those of the γ_{11n} arrays. The first one, the γ_{111} array (that is n=1) is in fact the Wenner-γ array, a traditional array. The last one, the γ_{n11} array where n=inf. is a null-array, the Midpoint-null or MAN array (Szalai *et al*. 2004). The γ_{811} array is one of the series of the γ_{n11} arrays between the traditional and the null array. Similar arrays (n=1-7), which have similar nPS maps are investigated in this paper. Below each nPS map its maximal value is shown. It is well seen that while the γ_{111} array's value is in the same order than those of the values of the first row arrays the maximal values of the γ_{n11} nPS maps are drastically increasing with increasing n. This high sensitivity motivated us to study the depth of detectability (DD) value of these arrays.

b.) The calculations of the depth of detectability (DD) values by Szalai *et al.* (2013b) has shown that the DD values of the γ_{11n} configurations can be 2-2.5 times larger than that of the best traditional configuration. A square resistive prism (e.g. 2 times 2m cross-section, 200 Ωm resistivity in a host of 100 Ωm) proved to be detectable from 14m depth (upper side of the prism) assuming 5% noise level and using γ_{113} configuration while it was detectable by the best traditional configuration, the P-Dp one, only from 6.6m depth. In the investigation 100 electrodes were applied with 1m electrode distance. Applying these configurations one could therefore get information from a larger depth which can be especially important in areas where the space available for measurements is limited, e.g. in built-in areas.

c.) It was shown comparing Szalai *et al*. (2011) and Szalai *et al.* (2013a) that the higher the DD value of a configuration, the better are its imaging features. Among the traditional configurations the DD value of the β-type configurations (Dp-Dp, P-Dp, Stummer, Wenner-β, electrode sequence is CCPP), was generally larger than those of the other configurations (Szalai *et al*. 2011). According to the imaging capacity the sequence of the investigated configurations was: Stummer, Dp-Dp, Wenner-β, P-Dp, Wenner-α, P-P too (Szalai *et al.* 2013a). That is the (β-type) configurations which have larger DD values proved to have better imaging capacity.

Concluding from a., b. and c. one can say that larger nPS_{max} value may lead to larger DD values which may result in better imaging capacity. The high nPS_{max} values of the γ_{11n} configurations could therefore result in good imaging features of these configurations.

d.) Szalai *et al*. (2002) and Falco *et al.* (2013) have demonstrated that geometrical null arrays (null arrays which provide zero signal in homogeneous half-space due to the appropriate positioning of the electrodes) can be very effective in field conditions. There is only one geometrical null array which can be built in 2D multielectrode systems, the MAN array (Szalai *et al.* 2004 and Fig. 1). The applicability of the commercial software to invert its data is very limited yet or not possible, while γ_{11n} configuration data may be inverted among certain conditions. Due to the MAN array is a special case of this array type if *n* is infinite (see Fig 1) the investigation of γ_{11n} arrays can be very useful to progress in understanding better the MAN array, as well.

e.) According to numerical calculations by Szalai *et al.* (2004) even the signal strength of the γ_{11n} arrays may be larger than that of the traditional arrays. About a dyke for example, with increasing depth the size of the anomaly was 50 Ωm, 20 Ωm and 12 Ωm with the most appropriate array lengths for the Wenner-α array, while it was about 60 Ωm, 36 Ωm and 32 Ωm for the MAN array, accordingly. It can be clearly seen that with the increasing depth of the dyke the MAN array's signal strength became even better and better in comparison with that of the traditional array. Even in field situation, in Finland, although the traditional Wenner-α array had larger signal strength both the MAN (it was called Midpoint null array) and the Wenner-γ null arrays produced larger anomalies due to horizontal resistivity changes (Szalai *et al.* 2004).

On the basis of these experiences, the study of the $\gamma(m)_{11n}$ configurations seems to be very reasonable.

To understand these arrays it is very important to see that they used to produce very sharp anomalies as can be expected on the basis of Figure 2 and as it was verified in both numerical investigations and field measurements (Szalai *et al*, 2004). It means that their anomalies are very sensitive to the horizontal resistivity changes. Aside from one-dimensional investigations, where the resistivity values supposed to change only in vertical direction this is one of the most important factors of the imaging.

Unfortunately the commercial inversion softwares are not able to maintain such sharp anomalies therefore the information which is contained in the measured data cannot be obtained. This is why in this paper mostly inhomogenities with small impact on the surface potential distribution are studied. In this way the gradient of the signal will be not as large and therefore more easily followed by the inversion. The other reason to investigate such inhomogeneities is that the traditional arrays produce acceptable results for large impact inhomogeneities therefore for such problems the application of other configurations is not required. In the future first a coarse image could be obtained by a traditional configuration which could later serve as a priori model for $\gamma(m)_{11n}$ configurations to refine the inverted images.

NUMERICAL INVESTIGATIONS

The investigated configurations

The results obtained by the γ_{11n} (Fig. 1) and their mirrored version, the γm_{11n} configurations were compared in the paper with the results of traditionally used configurations like the dipole-dipole (Dp-Dp), pole-dipole (P-Dp), Wenner-α and the optimised Stummer ones (Fig. 3).

In the investigation configurations with 60 electrodes were used with 1m electrode spacing excluding the Stummer configuration. Because the Stummer configuration is available only for 30 electrodes (Stummer *et al* 2004) 2m electrode distance was used to get the same configuration length as for the other configurations. The number of its data points is even in this case greater than that of any $\gamma(m)_{11n}$ configurations excluding only the γm_{112} one (see Figs. 3 and 4). It has also to be noted that in spite of the same change the Stummer configuration proved to be the best traditional configuration in the investigations by Szalai *et al* (2013). It is also possible that the imaging quality of the Stummer configuration could be further improved by using the same electrode distance as for the other configurations, but it would lead to significant increase of the data number. Besides this the imaging quality of the $\gamma(m)_{11n}$ configurations could most likely be improved by combining them.

The Dp-Dp configuration was used because it proved to be the best traditional configuration in the investigations by Szalai *et al. (*2013a). The P-Dp was applied because it is a three-electrode array like the MAN array and the γ_{11n} arrays themselves are getting closer and closer to be three-electrode arrays with the increasing number of *n*. Wenner-α configuration was chosen because it is one of the most popular and best known configurations, while the Stummer configuration (Stummer *et al.* 2004) should have to be the best conventional configuration because it was constructed using an optimisation process. Comparing the γ_{11n} and γ_{m11n} results with the results of these configurations one can get therefore an oversight about the abilities of them.

In Figure 6 the results of γ_{11n} configurations only for *n*=1-4 are shown which gives satisfactory information. In Figures 8 and 9 at the same time the whole series of γ_{11n} configurations (*n*=1-7) is presented to have an oversight about all these configurations. *n* is limited to 7 because its further increase leads to too less data points. *m* was 1-14, 1-11, 1-9, 1-7, 1-7 and 1-7 for the γ_{11n} configurations for *n*=2-7 (Fig. 1), accordingly.

The parameters for the traditional configurations are seen in Fig. 3. The configurations used in the optimised Stummer configuration can be found in Stummer *et al.* (2004).

The data coverage and number of data points are seen in Figure 3 for the traditional and in Figure 4 for the γ_{11n}, γ_{n11} and γm_{11n} configurations (n=2-7). While the Wenner-α and γ_{111} (Wenner-γ) configurations have only 570 data points, the Stummer configuration has 669, the Dp-Dp configuration 736 the P-Dp configuration 871 ones. In contrary to these configurations the γ_{11n} configurations (Fig. 3) have no more than 420 data points, that is their measuring time is significantly less, than those of the traditional configurations. Increasing *n* the number of data points is even decreasing drastically. The mirrored version of the γ_{11n} configurations contain two times as many point as its original version, but even in this case the number of the data points are only 840, 660, 540, 448, 392 and 342 for *n*=2-7, accordingly. It means that disregarding from γm_{112} configuration even the mirrored configurations have less data points, that is their measuring time is shorter, than that of the Stummer, Dp-Dp and P-Dp configurations (which used to produce the best results among the traditional configurations according to Szalai *et al.* 2013a).

Inversion parameters

All numerical calculations presented in this article were carried out by EarthImager, Version 2.1.6 (EarthImager, 2006). The parameters which are different from the software's basic parameters are summarized in Table 1. The basic parameters were only changed if it was necessary to get reasonable results. For e.g. the *Minimum Apparent Resistivity* parameters negative resistivity values were selected, because the signal may change its sign. To create Figure 6 *Pseudosection* was applied in the inversion process as *Starting Model* that is the section which contains the "measured" data. In all inversion process 1% Gaussian noise was added to the data (with the exclusion of the inversion whose results are presented in Figure 6) and RMS and L2 norm was used to study the data misfit. L2 norm is defined as the sum of the squared weighted data errors (difference between predicted/calculated and observed/measured resistivities). The RMS (root mean squared) error is its normalised version which takes into account also the data number.

Finite element method (FEM) was used in the modeling which is a numerical technique for finding approximate solutions to boundary value problems for differential equations. It uses variational methods to minimize an error function and produce a stable solution. FEM connects many simple element equations over many small subdomains, named finite elements, to approximate a more complex equation over a larger domain. FEM produces more accurate forward modeling solution than the finite difference method.

In many cases it would be possible to get better results than the ones presented by taking the images from other iteration steps. The selection of the most appropriate inverted section requires however knowledge of the model (which was used to calculate synthetic data) because the decrease of the RMS does not inevitably result in better images. In field measurements this knowledge is certainly not available although the final aim of such studies (including numerical investigations) is checking the applicability of different configurations in the field. Therefore field data processing requires a more or less automatic inversion. This is why *Stop RMS error option* was activated (values shown in Table 1) which completed the inversion in many cases after the 1st or 2nd iteration. It was also important to apply the same inversion parameters to all configurations to get (automatic) objective results making it possible to compare them.

RMS and L2 may not always be adequate to estimate the image quality. Often images with smaller (that is better) RMS and L2 proved to be worse because they contained more pseudo anomalies and more significant (therefore more disturbing) ones and the shape of the anomaly was also further from the model. The RMS and L2 are severely influenced by the resistivity values themselves and they may not be as sensitive to the geometrical parameters of the anomaly which is often more important. Therefore we prefer to qualify the inverted image obtained from numerical investigations similarly to that presented in “The criteria to interpret the results” section.

For many $\gamma(m)_{11n}$ configurations and for many models RMS proved to be high. There are two main reasons:

- The denominator d_i^{Meas} in the RMS function may be very small for many data, even close to zero due to that the signal may change its sign (Szalai *et al.*, 2004). It leads to very large values for individual measurements and therefore their sum, the RMS may also be large.

- The numerator may also be large for the same data point due to the rapid changes of the signal close to these small values. In a theoretical case if the predicted and measured curves (for a given depth) would be the same but would be slightly shifted horizontally from each other one would get very large RMS. This is not the case for the traditional configurations where the horizontal gradient of the signal is much smaller.

RMS and L2 are therefore not always appropriate values to estimate the quality of $\gamma(m)_{11n}$ measurements. Another value should be found to quantitatively estimate the quality of $\gamma(m)_{11n}$.

In the present article several models were numerically studied which aimed to illustrate 1. the effect of the resistivity contrast to the inverted image; 2. the horizontal- and 3. vertical resolution capacity of the different configurations; 4. the applicability of these configurations for larger effect anomalies and 5. the applicability for a realistic model.

The criterias to interpret the results

In the qualification and comparison of the results obtained by different configurations the main point (1a.) is whether the model body can be seen, that is whether is there an anomaly where the body should appear. Only if there is an anomaly there is a sense to continue the interpretation. In this case the next point (1b.) is whether are there any other (so-called pseudo) anomalies which are not awaited to be there and how much they influence the interpretation. The larger they are in their extension and/or in their resistivity contrast to the background value the more they can mislead the interpretation. If the body is detectable in the following the horizontal (2a.) and vertical (2b.) positions of the anomaly, its size (2c.), its resistivity value (2d.) and in ideal case its shape (2e.) can be compared to the model parameters and be taken into account in the interpretation.

In our investigations, however, where the aim was to investigate small impact model bodies the principal question had to be whether the anomaly due to the model will at least appear on the inverted image. This was the case e.g. in Figure 6. In case if there are more model bodies their separability (3.) can be an important item, too. This is the case in the resolution investigations in Figures 8. and 9 and also in Figure 10. If the bodies are separated from each other in the inverted image the same questions (1.a, b and 2.a,b,c,d,e) can be regarded like for the single bodies.

Results of the numerical investigations and their interpretation

Before going into the details of the numerical simulations, we explain why γm_{11n} configuration results will be presented instead of or beside γ_{11n} configurations. Figure 5 shows γ_{116}-, and γm_{116} images for a model containing three conductive prisms. Their resistivities are 10 Ωm in the 100 Ωm resistivity half-space. It is easy to see that the γm_{116} configuration is able to separate the prisms from each other better than the γ_{116} configuration by itself. Especially the prisms in the right side separate from each other very well. The effect of the prism in the middle of the section is also more remarkable in the γm_{116} image.

Investigations of further models not presented here motivated us to use the γm_{11n} configurations. They produced better images than the γ_{116} configurations, especially if the inhomogeities are in deeper parts of the model. This is the reason we prefer to use the mirrored version of these configurations. In the present stage of the investigations, it seems, however, to be reasonable to present also the γ_{116} results, at least for a few models.

The results of DD investigations by Szalai *et al.* (2013b) and MAN configuration studies (Szalai *et al.*, 2004) referred to the usefulness of the γ_{11n} configurations especially if the effect of the inhomogeneity is small, that is if its size/depth ratio and/or its resistivity contrast to the host is small. At first the image of a small size prism will be compared with those of the often applied dipole-dipole (Dp-Dp), pole-dipole (P-Dp), optimised Stummer (St) and γ_{11n} (*n*=1-4) configuration's images (Fig. 6).

While the resistivity of the host in Figure 6 was 100 Ωm, the resistivities of the prism were 500, 160 and 140 Ωm in the columns in Figure 6. The depth of the upper side of the prism is 3.9 m, its thickness is 2.0 m, and its horizontal extension is 2.5 m, between 26.5 and 29 m. For the applied inversion parameters see Table 1.

If the resistivity of the prism was 500 Ωm (Fig. 6, left column), that is the resistivity contrast to the background was significant the prism proved to be detectable by each configurations, however the application of the γ_{111} configuration is not suggested due to the significant artefacts which are in the same resistivity range than the “real” anomaly itself. The other configurations detect the model clearly, they position it correctly and the pseudoanomalies were not comparable to the real anomaly. The size of the anomaly is, however, larger than expected.

The conventional configurations proved to be better for this model because the effect of the anomaly is large due to the large resistivity contrast between the model and the background. For such models they work properly, while the inversion of the $\gamma(m)_{11n}$ configuration data for large effect inhomogeneities is not well resolved yet.

For the 160 Ωm prism (Fig. 6, middle column) only the γ_{113}-, and γ_{114} configuration images are somewhat convincing, while the traditional configurations proved to be rather ineffective. The γ_{113}, and γ_{114} images present a resistive anomaly at the right position which arises quite characteristically from the background and the artefacts are smaller in their size than the anomaly. The γ_{114} configuration results are the most convincing from the whole series, although the anomaly is not at all sharp in its case, neither.

Finally the 140 Ωm prism (Fig. 6, right column) was detectable by all configurations excluding the Stummer one, but the anomalies were more or less mispositioned. The γ_{113} and the γ_{114} configurations seem to be the closest to the real model, although they, too, produced significant artefacts. The most important is however the presence of an anomaly at the position of the inhomogeneity which is inevitable for a correct interpretation.

Artefacts could nevertheless easily mislead the interpretation of field data. To avoid misinterpretation, however, there are several possibilities. If the location of the target is more or less known even images with artefacts enable its more precise localization and description. In this case the artefacts should not have taken into account. If there may be more prism-like objects and there is not any information regarding their position it is possible: 1. to compare data of different geoelectric configurations. If images of many configurations display an anomaly at the same position, it is highly probable that there is an inhomogeneity. If an anomaly appears on only 1-2 images, it is most likely an artefact. An anomaly with a large value and extension (e.g., on the γ_{114} image in the right column between about 34 and 44 m) does not have any pair on the γ_{112} or γ_{113} images. Therefore its validity is strongly questioned. In contrast, the anomaly in the middle of the section appears on all of these images (although not exactly at the same position) increasing the probability of the existence of an inhomogeneity there. The MOST algorithm (Leontarakis and Apostolopoulos (2012, 2013) basically uses the same principle. In this process, artefacts due to random noises eliminate each other while the anomalies due to real objects strengthen each other (see Fig. 7, discussed later more detailed). 2. Similar procedures can be applied carrying out measurements several times with the same configuration (stacking). 3. The comparison of geoelectric results with results of other geophysical measurements, or the joint inversion of different data sets could also decrease the uncertainty. 4. A direct investigation at the problematic places is also possible through excavations or boreholes. Which of these procedures is applied it is a question of money.

While for the models with high resistivity contrast (500 Ωm) the traditional configurations proved to be better their quality decreases faster with the decreasing resistivity contrast than that of the γ_{11n} configurations. In the small resistivity contrast range the application of the γ_{11n} configurations seem to be more worthwhile and the quality of their image can be further improved by the Model Stacking (MOST) procedure introduced by Leontarakis and Apostolopoulos (2012, 2013). Stacking the models of different configurations the model of the combined configuration leads to a final model almost free of artefacts with extremely high resolution in shape and positioning, and an intense representation of the targets. The Model Stacking procedure is based on a simple statistical approach, calculating the geometric mean of the different values, which are given by each model for the same point of the half-space (Leontarakis and Apostolopoulos, 2012, 2013).

The RMS error values for the images in Figure 6 were between 4.2 and 5.2% for all configurations, that is in this sense there was not any significant difference among the investigated configurations.

Figure 7 presents the effect of the MOST procedure. In the first row ~~in Figure 7~~ the MOST results made of the combination of the P-Dp and Dp-Dp configuration results are shown for both the 160 Ωm and 140 Ωm prism models. This configuration combination contains 1540 data points. For the 160 Ωm prism the MOST result is more convincing than the results of the simultaneous configurations (Fig. 6), but it still contains a lot of artefacts. The MOST result made of the $\gamma_{112,}$ γ_{113} and γ_{114} configurations (Fig. 7, second row) is much more convincing in spite of that this combination contains only about 30% less, 1020 data points. The resistivity values of the artefacts are in this case not comparable with that of the real anomaly and it became sharper and more characteristic than in the individual images (Fig. 6). The quality of the image could be even further improved by stacking all of these configurations (Fig. 7, third row), but thus the measurement becomes less economic.

The situation is about the same for the 140 Ωm prism model (Fig. 7, right column). The MOST procedure led to reasonable image for both (traditional-, and γ_{11n}-) configuration combinations. In this case even the combination of all configurations (Fig. 7, third row) seem to be reasonable if the aim is to get high quality image even among very wrong conditions. Disregarding from the artefact at the end of the profile the prism was clearly detected in this way and its all geometrical parameters that are its horizontal and vertical positions and even its size are satisfactory.

If artefacts do not disappear even after carrying out the MOST procedure it is still possible to use other geophysical techniques or apply direct procedures to decrease the uncertanity of the interpretation.

Summarising the results of Figures 6 and 7 it can be stated that while the traditional Dp-Dp-, and Stummer configurations proved to be well usable if the resistivity contrast was larger (500 Ωm), the γ_{11n} configurations proved to be more and more fruitful in comparison with the traditional configurations if the contrast was smaller (160, 140 Ωm). The advantageous features of the γ_{11n} configurations became especially spectacular by combining them using the MOST procedure. The application of the γ_{11n} configurations and applying the MOST procedure is therefore highly recommended in case if a small impact anomaly should be found in a noisy environment.

In the proceeding Figures only Wenner-α and Stummer configuration results will be shown from the traditional ones, because we wanted to compare our results with the results of a popular traditional configuration (W-α) and with that of the best traditional configuration (St). At this stage of the studies we found important to present also the γ_{11n} configuration results beside of the γm_{11n} configuration ones.

Figure 8 presents the horizontal resolution capacity of the Wenner-α, Stummer-, γ_{11n}-, and γm_{11n} (*n*=1-7) configurations. For the applied inversion parameters see Table 1. The model parameters are presented on the top of Figure 8. The Wenner-α configuration was unable to separate the conductive prisms from each other. The Stummer configuration clearly separates the right hand prism from the others and the separateness of the second prism from the right side may be supposed, too. The γ_{11n}-, and γm_{11n} configurations (from *n*=2) separate the prism farthest on the right from the others even more convincingly creating a high resistivity region (29-38m) between the prisms. With increasing *n* the second prism from the right side separates itself more convincingly from the other prisms (there is again a high resistivity zone between 18m and 22m). The first two bodies in the left side - whose distance is comparable to their depth (4m versus 4.9m) - could not have been separated from each other by neither of the studied configurations. From the point of view of their horizontal resolution capacity, both the γm_{11n}-, and the γ_{11n} configurations proved to be definitely better than even the optimised Stummer configuration, not speaking about the Wenner-α configuration. The RMS value was below 2% for each configurations.

Figure 9 demonstrates the results of vertical resolution investigations for the same configurations. For the applied inversion parameters see Table 1. The model parameters are given on the top of Figure 9. All prisms closer to the surface were detected by each configuration. The Stummer and the $\gamma(m)_{11n}$ (n=1,2) configurations proved to be almost perfect regarding all quality parameters. The near-surface anomalies of the W-α and the other $\gamma(m)_{11n}$ configurations are not as sharply delineated, but they are satisfactory, too.

For the prisms on deeper levels, only the one on the right side was observed by all configurations (excluding only the γ_{117} configuration), but it merged into the one above it because they are too close to each other.

From the prism pair on the left side, the deeper one proved to be almost undetectable even by the Stummer configuration. In contrary, most $\gamma(m)_{11n}$ results refer to the existence of the deeper prism. They show a long, narrow anomaly downwards (e.g. γ_{115}, γ_{116} and γm_{117} configurations) or even an anomaly which delineates well the prism pair below each other (e.g. $\gamma_{117,}$ γm_{113} and γm_{114} configurations). The W-α configuration indicates the deeper anomaly, as well, but with a very wide and uncertain anomaly.

The Stummer configuration indicates weakly the existence of the deeper prism in the middle of the section by, but the anomalies produced by the $\gamma_{113,}$ $\gamma_{116,}$ $\gamma m_{116,}$ γm_{117} configurations and especially that of the γm_{113} configuration are more convincing. Their anomalies are narrower and/or get closer to the depth of the deeper prism and/or the values of the anomalies differs more from the background value.

For this model the RMS values of the γ_{11n}-/γm_{11n} configurations from n=3 were systematically much larger (20-32%) than those of the traditional configurations (below 2%). As it has however already been mentioned the principal question is the similarity of the inverted image to the reality which is the model in numerical investigations. RMS value seems increase with increasing n in this model. It may happen because with increasing n the arrays approach the null array situation and produce sharper and sharper anomalies.

The separation of the prisms below each other was impossible for all the configurations we studied, but certain γ_{11n}- and γm_{11n} configurations and especially the γm_{113} configuration proved to be better in detection of the deeper bodies.

Next we investigated a model which did not seem to be favourable for the γm_{11n} configurations (Fig. 10) because of the large size of the inhomogeneities (inversion parameters are in Table 1.).

The model in the left column of Figure 10 is very similar to the one studied by Wilkinson *et al.* (2006). Here the anomalous bodies with large resistivity contrast (100 Ωm in comparison to the 10 Ωm half-space value) and the large size can be seen better in the Stummer image than in most γm_{11n} configuration images. Although the deepest (from the detectability point of view) most critical body is displayed more convincingly by the γm_{11n} (n=2-6) configurations these images contain several pseudoanomalies, as well. In such a case again a solution similar to the one applied by Leontarakis and Apostolopoulos (2012, 2013) could be suggested to supress the pseudoanomalies and highlight the real anomalies. We would like to call your attention also to the γm_{112} configuration which gives - in spite of its higher RMS value - the most characteristic image of the prisms disregarding from the pseudoanomaly in the left bottom part of the section.

If however the near-surface bodies are not present (Fig. 10 middle column), all γm_{11n} configurations give better results than the Stummer configuration. They can separate the two deeper bodies from each other more impressively. It is especially true if n is at least 3. The γm_{11n} images remain as impressive even in the presence of near-surface bodies if they do not influence to the surface potential too much (Fig. 10 right column). It is remarkable that also the near-surface bodies are presented more convincingly by the γ_{11n}-, than by the traditional configurations. The γm_{116} configuration produced the best image which resembles the best to the model. It separated all prisms unambiguously from each other, their horizontal positioning was perfect, their vertical positioning was reasonable, like that of their shape. Of course due to their limited effect to the surface potential the resistivity values of the anomalies may not be very good.

We found that γ_{11n} and γm_{11n} configurations may be more productive even in the investigation of bodies which have larger effect to the potential distribution.

At last Figure 11 demonstrates a realistic example (inversion parameters are in Table 1): a hole in the liner on the bottom of a waste deposit. On the basis of the former results we did not find important to show the γ_{111} result in this case. The liner's resistivity was supposed to be 10000 Ωm, while the background's was supposed to be 100 Ωm. The liner on the bottom of the waste deposit used to be namely a kind of plastic which has a very high resistivity value. The hole was supposed - for simplicity reasons - to have the same resistivity like that of the "waste" itself and the rock below the waste deposit. It is a simple model for the given situation, but it is able to handle the main point of the problem, the detectability of the hole and its positioning.

In this case the fundamental question is whether there is a hole in the liner. Regarding this question all configurations with the exception of the W-α proved to be satisfactory, because all of them presented a conductive anomaly close to the expected position which refers to the existence of a hole in the resistive liner. Regarding the second most important question, the horizontal position of the hole, in case of the γ_{m11n} configurations (n=5-7) the hole is although horizontally in the middle of the conductive anomaly, but its horizontal extension is much larger than that of the body's. The Stummer configuration indicates a discontinuity in the resistive layer, but it is strongly mispositioned and much wider than the hole that is the Stummer configuration was not able to localize it precisely. In contrary the γ_{m11n} configurations (n=2-4) and especially the γ_{m112} and γ_{m113} ones produced narrow anomalies at the right location. These configurations seem therefore to be convenient to detect a hole and to localize it to fulfill the most principal tasks.

Although it is not important from the point of view of the given problem, we note that the segment below the liner is resistive in the inverted section due to the fact that the current is not able to penetrate below the resistive liner. Regarding it differently the whole bottom part of the section below the liner would be most likely below the DOI (depth of investigation) level introduced by Oldenburg and Li (1999) because the DOI level used to be closer to the surface where there are bodies with large resistivity contrast to the average values. It refers in turn to the fact that below this level surface data are insensitive to the value of the physical property of the earth.

CONCLUSIONS

A new configuration type, the γ_{11n} configurations are introduced, which have not been investigated yet. Our numerous former studies let us assume that such so-called quasi null configurations can be very useful complements to the traditional configurations.

Numerical investigations showed that although models which have large impact to the surface potential were presented better by the traditional configurations the quality of their image decreases faster with decreasing model impact than that of the γ_{11n} configurations. For small impact models the application of the γ_{11n} configurations is worthwhile at least together with a traditional configuration. It was shown that the quality of the image of $\gamma(m)_{11n}$ configurations can even be further improved by the Model Stacking procedure resulting a good image even for small-effect models. If the application of the MOST procedure does not help avoid the uncertainties, then a combination of the geoelectric results with results of other geophysical investigations, or direct investigation of the possible inhomogeneities is recommended.

Most of the γ_{11n} configurations proved to be definitely better than those of the traditional configurations in horizontal resolution investigations (especially with larger *n* values.) The mirrored version of the γ_{11n} configurations (the γm_{11n} configurations) were even better than the original configurations.

Although in the vertical resolution studies the separation of the anomalies directly below each other proved to be impossible for all studied configurations, certain $\gamma(m)_{11n}$ configurations and especially the γm_{113} configuration proved to be good in detection of the deeper bodies.

For certain models γm_{11n} configurations may be better even in case of large-impact inhomogeneities, as it was illustrated, too. The γm_{11n} configurations proved to be better than even the Stummer configuration also in detection and positioning of a hole in the liner in a realistic field example.

Summarising the numerical results it can be stated that the $\gamma(m)_{11n}$ configurations are more sensible to small impact models, than the traditional configurations, including the optimised Stummer configuration, giving better image about them. They proved to have better horizontal resolution, as well. In case of model bodies below each other many of them were able to indicate the existence of the lower body and even its vertical position in contrary to the traditional configurations. It is in accordance with the larger depth of detectability values of these configurations which were calculated by Szalai *et al*. (2014). These statements are right in spite of the smaller data coverage of these configurations which could however be increased by the simultaneous use of different $\gamma(m)_{11n}$ configurations. Applying the Model Stacking procedure by combining the images of several $\gamma(m)_{11n}$ configurations the results could even be further improved.

In the present paper we mostly concentrated on models which seem to be most promising for the γ_{11n} and γm_{11n} configurations, according to our theoretical considerations. On the basis of these investigations we propose that problems like detection and characterisation of tunnels, caves, cables, tubes, abandoned riverbeds, lack of continuity in clay layers could be effectively solved by these configurations. Their use is also recommended in problems where false alarms are less important than high resolution, e.g. in dam investigations or waste deposit monitoring. They can be useful in any problems where small changes are expected with time, e.g. in any monitoring problems. Due to the reduced effect of the inhomogeneity below conductive or resistive layers, the $\gamma(m)_{11n}$ configurations should be effective in such problems.

They can be especially productive in comparison to other configurations in areas where the space available for measurements is limited.

The time required for measurements with the $\gamma(m)_{11n}$ configuration is moreover less than that of the traditional configurations, because disregarding from the γm_{112} configuration they contain less data points, than the traditional configurations. The combined application of different $\gamma(m)_{11n}$ configurations is rather economic and it can highly improve the efficiency of the measurements. A combination with traditional array results or with results of other geophysical measurements can also make it very straightforward to get the best possible interpretation.

We think on the basis of the presented investigations that the $\gamma(m)_{11n}$ configurations might give significant contribution to the geoelectric method. Their further study is therefore highly recommended.

REFERENCES

Alpin L.M., Berdichevskii M.N., Vedrintsev G.A. and Zagarmistr A.M. 1966. Dipole methods for measuring earth conductivity, Consultants Bureau, New York, p. 302.

Butler D.K. 2005. Near-Surface Geophysics. SEG, Tulsa, Oklahoma, USA, p. 355.

Clark A. J. 1990. *Seeing Beneath the Soil*. B.T. Batshford Ltd. London, p. 176.

EarthImager. 2006. *2D Resistivity and IP Inversion Software*, Instruction Manual, Advanced Geosciences, Inc. Austin, Texas, p. 137.

Edwards L. S. 1977. A modified pseudosection for resistivity and induced-polarization. *Geophysics*, 42, 1020-1036.

Falco P., Negro F., Szalai S., Milnes E. 2013. Fracture characterisation using geoelectric null-configurations, *Journal of Applied Geophysics,* 93, 33-42

Furman A., Ferré T.P.A., Warrick A.W. 2003. A Sensitivity Analysis of Electrical Resistance-Tomography Array Types Using Analytical Element Modeling, *Vadose Zone Journal*, 2, 416-423

Furman A., Ferré T.P.A., Warrick A.W. 2004. Optimization of ERT surveys for monitoring transient hydrological events using perturbation sensitivity and genetic algorithms, Vadose Zone Journal, Vol. 3, pp. 1230-1239.

Kirsch R. 2006. *Groundwater Geophysics*. Springer, p. 493.

Knödel K., Krummel H. and Lange G. 2005. *Band 3. Handbuch zur Erkundung des Untergrundes von Deponien und Altlasten, 2nd ed.* Springer, p. 128.

Leontarakis K., Apostolopoulos G.V. 2012. Laboratory study of the cross-hole resistivity tomography: the Model Stacking (MOST) Technique. *Journal of Applied Geophysics,* 80, 67-82.

Leontarakis K., Apostolopoulos G.V. 2013. Model Stacking (MOST) technique applied in cross-hole ERT field data for the detection of Thessaloniki ancient walls' depth. *Journal of Applied Geophysics,* 93, 101-113.

Metwaly M., El-Qady G., Matsushima J., Szalai S., Al-Arifi N. S. N., Taha A. 2008. Contribution of 3-D electrical resistivity tomography for landmines detection, *Nonlin. Processes Geophys.,* 15, 977-986.

Oldenburg D.W., Li Y. 1999. Estimating depth of investigation in dc resistivity and IP surveys, *Geophysics*, 64 (2), 403–416.

Roy A., Apparao, A., 1971. Depth of investigation in direct current methods. *Geophysics*, 36, 943–959.

Stummer P., Maurer H., Green A.G., 2004. Experimental design: Electrical resistivity data sets that provide optimum subsurface information. *Geophysics*, 69 (1), 120–139, 10.1190/1.1649381

Szalai S., Koppán A., Szokoli K., Szarka L. (2013a): Geoelectric imaging properties of traditional arrays and of the optimized Stummer configuration, *Near-Surface Geophysics,* 11, 51-62.

Szalai S., Kósa I., Nagy T., Szarka L. (2009a): Effectivity enhancement of azimuthal geoelectric measurements in determination of multiple directions of subsurface fissures, on basis of analogue modelling experiments, 15th European Meeting of Environmental and Engineering Geophysics, Proceedings & Exhibitors' Catalogue Near Surface 2009, P25.

Szalai S., Lemperger I., Metwaly M., Kis Á., Wesztergom V., Szokoli K., Novák A. 2014. Multiplication of the depth of detectability using γ_{11n} arrays, *Journal of Applied Geophysics*, 107, 195-206.

Szalai S., Novák A., Szarka L. (2009b.) Depth of Investigation and vertical resolution of surface geoelectric arrays. *Journal of Engineering and Environmental Geophysics* 14, 15-23.

Szalai S., Novák A., Szark, L. 2011. Which geoelectric array sees the deepest in a noisy environment? Depth of detectability values of multielectrode systems for various two-dimensional models. *Physics and Chemistry of the Earth*, 36, 1398-1404.

Szalai S., Szarka L., Marquis G., Sailhac P., Kaikkonen P. and Lahti I. 2004. Colinear null arrays in geoelectrics. *Proceedings of the 17th S.3-P.3 IAGA WG 1.2 on Electromagnetic Induction in the Earth Workshop*, Hyderabad, India

Szalai S., Szarka L., Prácser E., Bosch F., Müller I., Turberg P., 2002. Geoelectric mapping of near-surface karstic fractures by using null-arrays: *Geophysics*, 67, 1769–1778.

Szalai S., Szarka L., 2008a. On the classification of surface geoelectric arrays. *Geophysical Prospecting,* 56, 159–175, doi: 10.1111/j.1365-2478.2007.00673.x.

Szalai S., Szarka L., 2008b. Parameter sensitivity maps of surface geoelectric arrays, I. linear arrays. *Acta Geod. Geoph. Hung*., 43 (4), 419–437, DOI: 10.1556/AGeod.43.2008.4.4

Szalai S., Szarka L., 2008c. Parameter sensitivity maps of surface geoelectric arrays, II. Nonlinear and focussed arrays. *Acta Geod. Geoph. Hung.,* 43 (4), 439–447, DOI: 10.1556/AGeod.43.2008.4.5

Van Nostrand R.G. and Cook K.L. 1966. Interpretation of Resistivity Data. Geological Survey professional paper 499. US Government Printing Office, Washington DC

Ward S. H. (1990): Geotechnical and environmental geophysics, Vol. I. Review and tutorial, SEG, Tulsa, Oklahoma

Wilkinson P.B., Meldrum P.I., Chambers J.E., Kuras O., Ogilvy R. D. (2006): Improved strategies for the automatic selection of optimised sets of electrical resistivity tomography measurement configurations, *Geophys. J. Int.,* 1119-1126.

Zhdanov M.S. and Keller G.V. 1993. *The Geoelectrical Methods in Geophysical Exploration*. Elsevier, p. 873.

FIGURE CAPTIONS

Figure 1: The γ_{11n} arrays. Stars denote current, circles denote potential electrodes; *a* is the electrode distance.

Figure 2: The normalised parameter sensitivity (nPS) maps of several traditional and typical γ_{n11} arrays in a depth of one tenth of the array length. Stars denote current, circles denote potential electrodes. Below the maps their maximal values can be seen.

Figure 3: Left side: the applied traditional configurations with their parameters. Stars denote current electrodes, full circles potential electrodes. Right side: Data coverage and number of data points for the same configurations.

Figure 4: Data coverage and number of data points for the γ_{11n}, γ_{n11} and γm_{11n} configurations (n=2-7).

Figure 5: Example to show the advantage of the mirrored configurations against the single ones. The model is given on the top of the figure. The resistivity of the prisms is 10 Ωm while the half-space resistivity is 100 Ωm.

Figure 6: Inverted sections for several traditional-, and γ_{11n} configurations. Resistivities of the prisms are 500, 160 and 140 Ωm. Background resistivity is 100 Ωm. The model is given on the top of the figure.

Figure 7: MOST images of different configuration combinations

Figure 8: Horizontal resolution investigation for different traditional-, and γ_{11n} configurations. The model is given in the first row.

Figure 9: Vertical resolution investigation for different traditional-, and γ_{11n} configurations. The model is given in the first row.

Figure 10: Left column: Inversion results from the Wenner-γ, Stummer and $\gamma(m)_{11n}$ (n=1-7) configurations for the model similar to that in Wilkinson *et al.* (2006). Middle column: results for the same model without the near-surface anomalous bodies. Right column: the first model with smaller near-surface inhomogeneities. The model is given in the first row.

Figure 11: The effect of a hole in the liner at the bottom of a waste deposit from different configurations. The uppermost Figure is the model we investigated.

TABLE CAPTIONS

Table 1 The parameters applied in the numerical investigations which are different from the basic (Surface) parameters of the EarthImager v2.1.6. software. The parameters different from the basic ones are written in bold.

ACKNOWLEDGEMENTS

S. Szalai, one of the authors of this paper is a grantee of the Bolyai János Scholarship. This study was supported by the TAMOP-4.2.2.C–11/1/KONV-2012-0015 (Earth-system) project sponsored by the EU and European Social Foundation. We are very grateful to the Associate Editor, Oliver Ritter and anonymous reviewers for enhancing the quality of this paper.

647

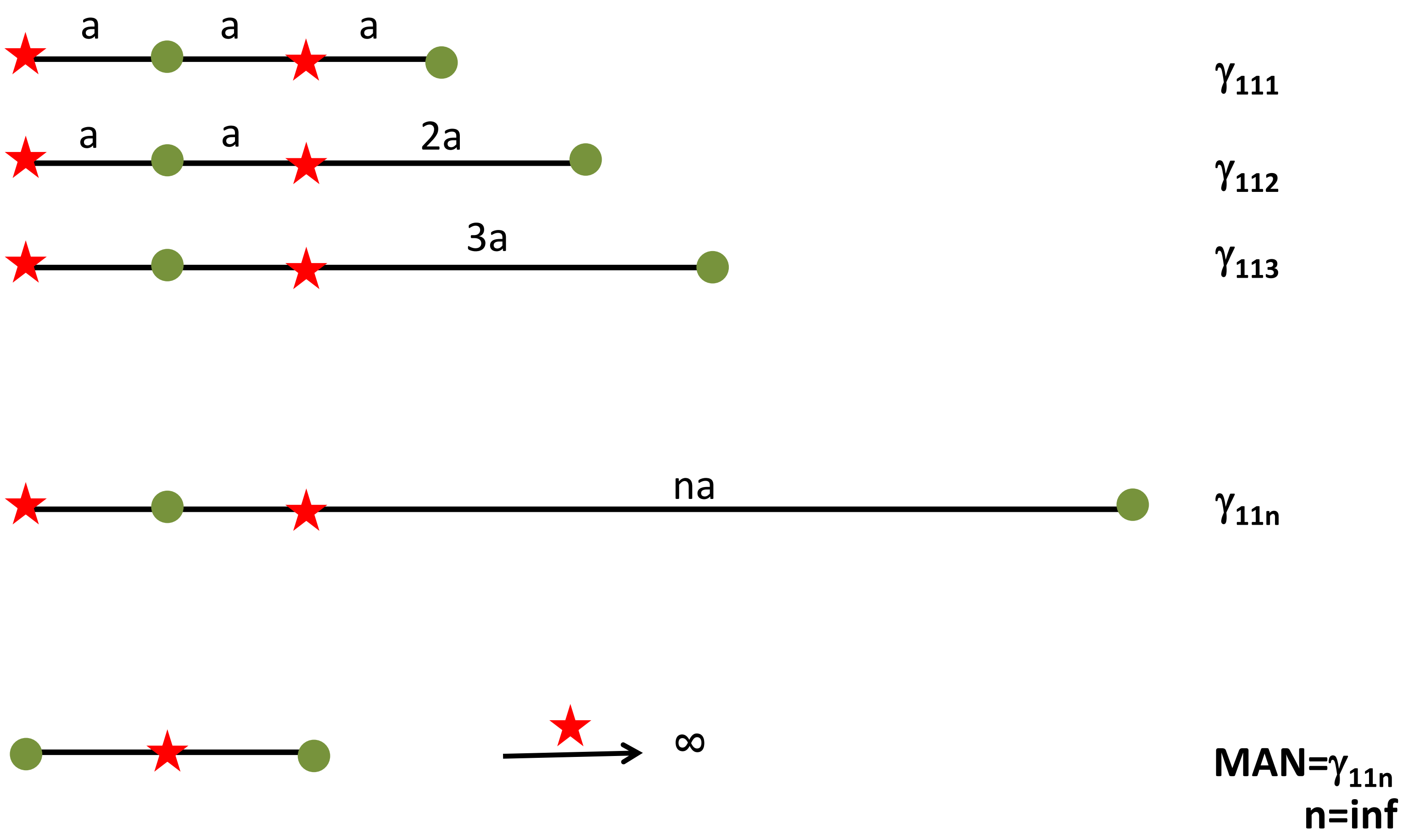
a
a
a
γ111
a
a
2a
γ112
3a
γ113
na
γ11n
∞
MAN=γ11n
n=inf

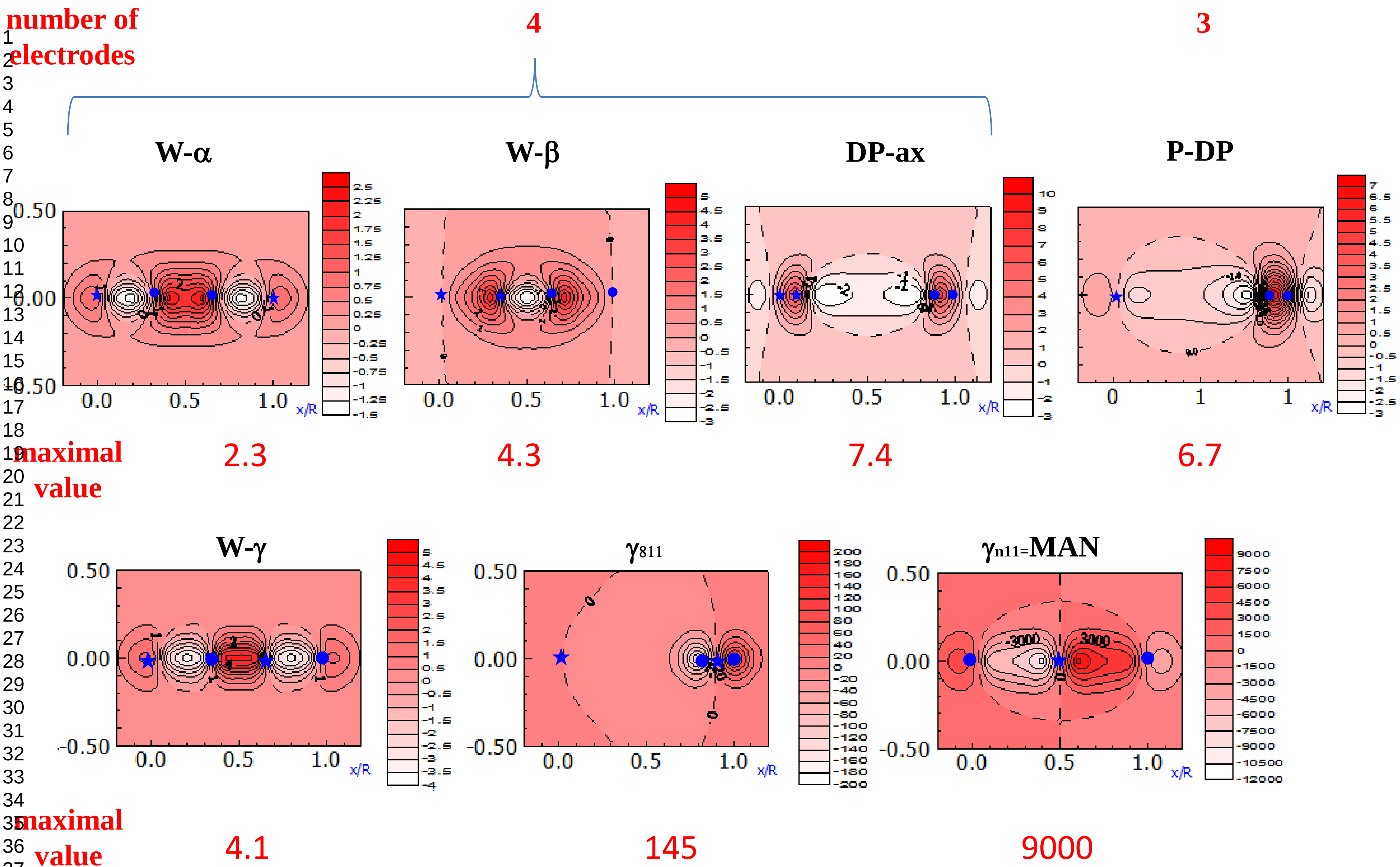
number of electrodes
4
3
W-α
W-β
DP-ax
P-DP
maximal value
2.3
4.3
7.4
6.7
W-γ
γ811
γn11=MAN
maximal value
4.1
145
9000
x/R

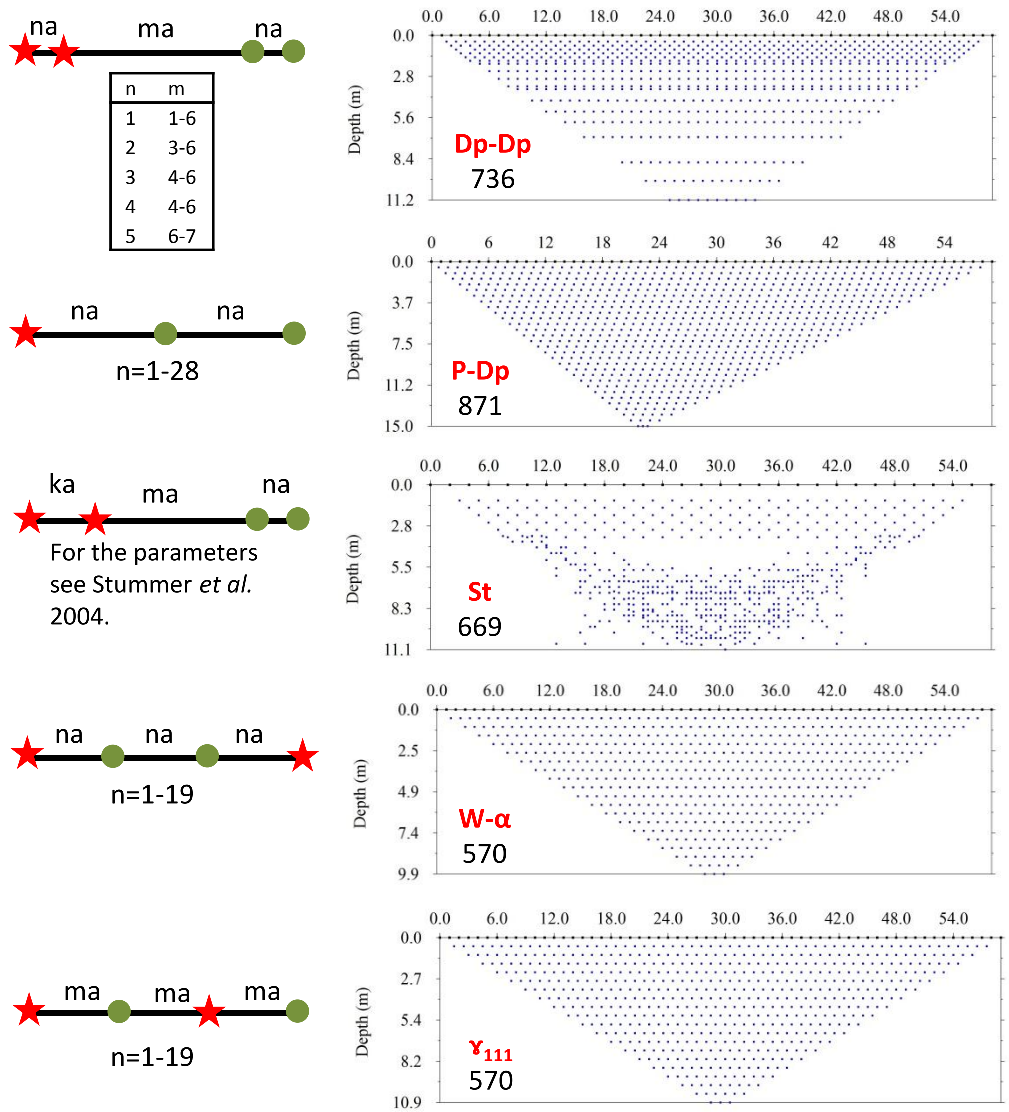
na ma na
n m
1 1-6
2 3-6
3 4-6
4 4-6
5 6-7
Dp-Dp
736
na na
n=1-28
P-Dp
871
ka ma na
For the parameters see Stummer et al. 2004.
St
669
na na na
n=1-19
W-α
570
ma ma ma
n=1-19
γ111
570
Depth (m)

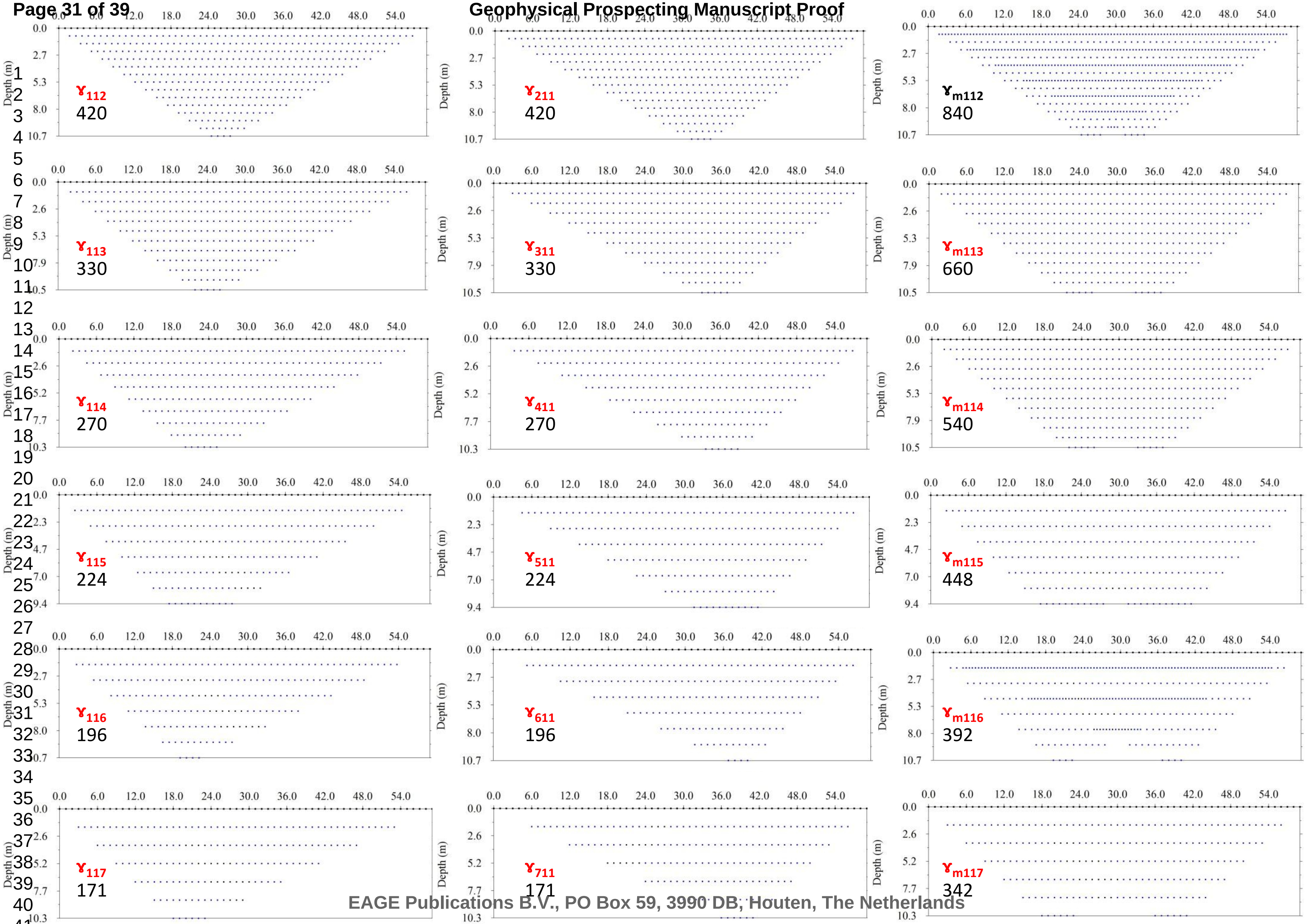
Depth (m)
ɣ112
420
ɣ211
420
ɣm112
840
ɣ113
330
ɣ311
330
ɣm113
660
ɣ114
270
ɣ411
270
ɣm114
540
ɣ115
224
ɣ511
224
ɣm115
448
ɣ116
196
ɣ611
196
ɣm116
392
ɣ117
171
ɣ711
171
ɣm117
342

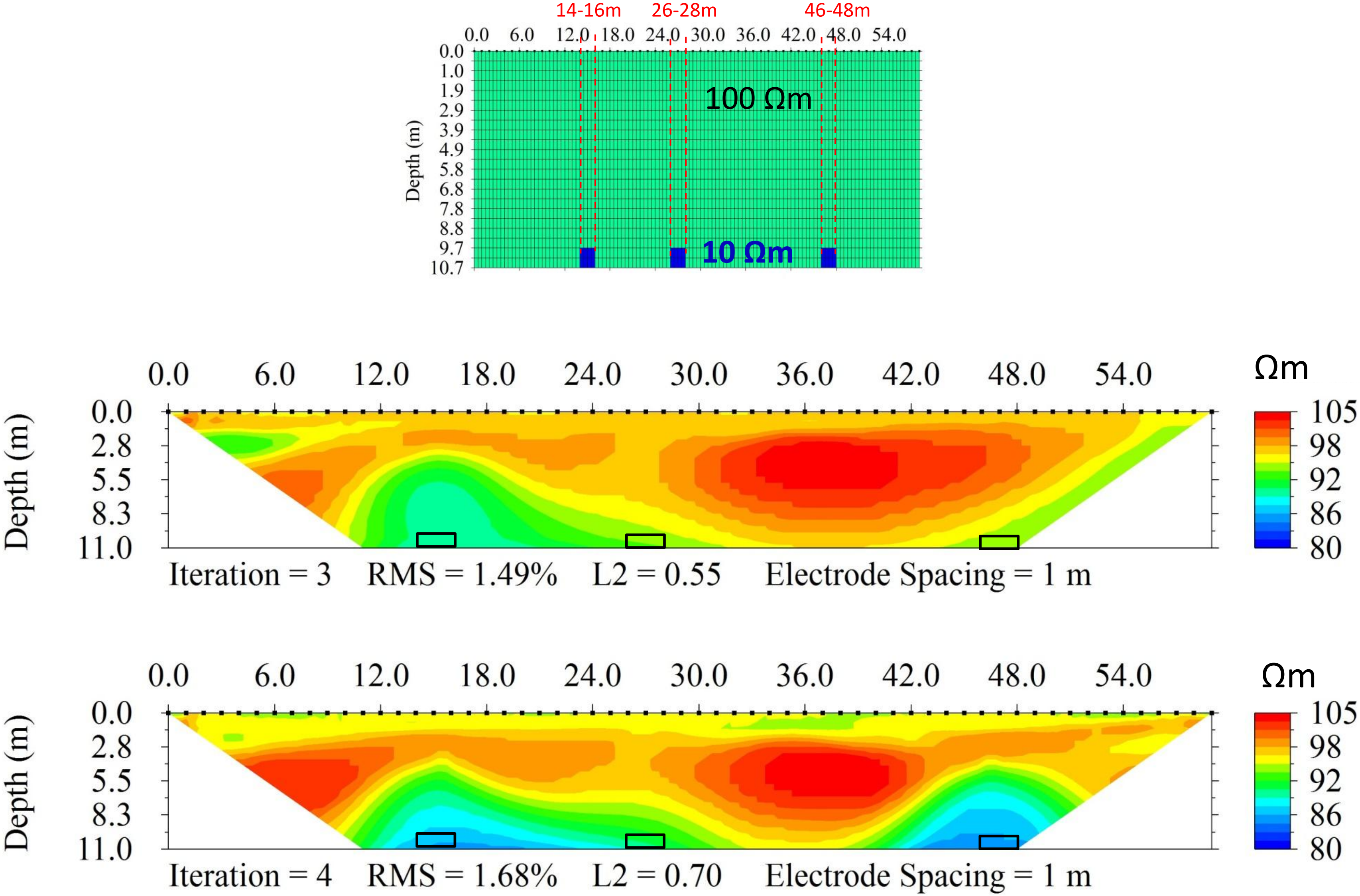
14-16m
26-28m
46-48m
0.0 6.0 12.0 18.0 24.0 30.0 36.0 42.0 48.0 54.0
Depth (m)
0.0 1.0 1.9 2.9 3.9 4.9 5.8 6.8 7.8 8.8 9.7 10.7
100 Ωm
10 Ωm
0.0 6.0 12.0 18.0 24.0 30.0 36.0 42.0 48.0 54.0
Depth (m)
0.0 2.8 5.5 8.3 11.0
Ωm
105 98 92 86 80
Iteration = 3 RMS = 1.49% L2 = 0.55 Electrode Spacing = 1 m
0.0 6.0 12.0 18.0 24.0 30.0 36.0 42.0 48.0 54.0
Depth (m)
0.0 2.8 5.5 8.3 11.0
Ωm
105 98 92 86 80
Iteration = 4 RMS = 1.68% L2 = 0.70 Electrode Spacing = 1 m

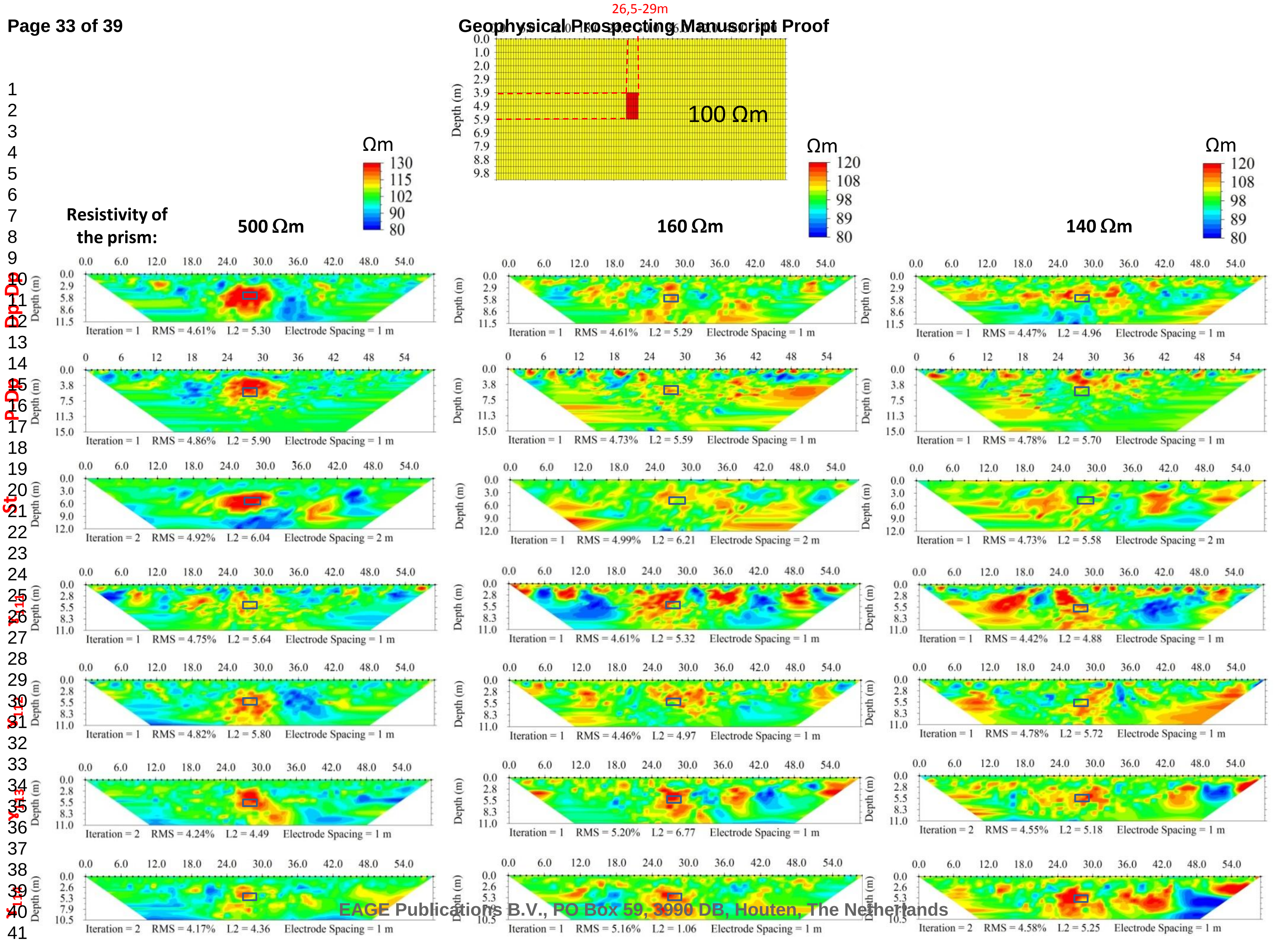
26,5-29m
Depth (m)
100 Ωm
Ωm
Resistivity of the prism:
500 Ωm
160 Ωm
140 Ωm
Dp-Dp
P-Dp
St
Iteration = 1 RMS = 4.61% L2 = 5.30 Electrode Spacing = 1 m
Iteration = 1 RMS = 4.61% L2 = 5.29 Electrode Spacing = 1 m
Iteration = 1 RMS = 4.47% L2 = 4.96 Electrode Spacing = 1 m
Iteration = 1 RMS = 4.86% L2 = 5.90 Electrode Spacing = 1 m
Iteration = 1 RMS = 4.73% L2 = 5.59 Electrode Spacing = 1 m
Iteration = 1 RMS = 4.78% L2 = 5.70 Electrode Spacing = 1 m
Iteration = 2 RMS = 4.92% L2 = 6.04 Electrode Spacing = 2 m
Iteration = 1 RMS = 4.99% L2 = 6.21 Electrode Spacing = 2 m
Iteration = 1 RMS = 4.73% L2 = 5.58 Electrode Spacing = 2 m
Iteration = 1 RMS = 4.75% L2 = 5.64 Electrode Spacing = 1 m
Iteration = 1 RMS = 4.61% L2 = 5.32 Electrode Spacing = 1 m
Iteration = 1 RMS = 4.42% L2 = 4.88 Electrode Spacing = 1 m
Iteration = 1 RMS = 4.82% L2 = 5.80 Electrode Spacing = 1 m
Iteration = 1 RMS = 4.46% L2 = 4.97 Electrode Spacing = 1 m
Iteration = 1 RMS = 4.78% L2 = 5.72 Electrode Spacing = 1 m
Iteration = 2 RMS = 4.24% L2 = 4.49 Electrode Spacing = 1 m
Iteration = 1 RMS = 5.20% L2 = 6.77 Electrode Spacing = 1 m
Iteration = 2 RMS = 4.55% L2 = 5.18 Electrode Spacing = 1 m
Iteration = 2 RMS = 4.17% L2 = 4.36 Electrode Spacing = 1 m
Iteration = 1 RMS = 5.16% L2 = 1.06 Electrode Spacing = 1 m
Iteration = 2 RMS = 4.58% L2 = 5.25 Electrode Spacing = 1 m

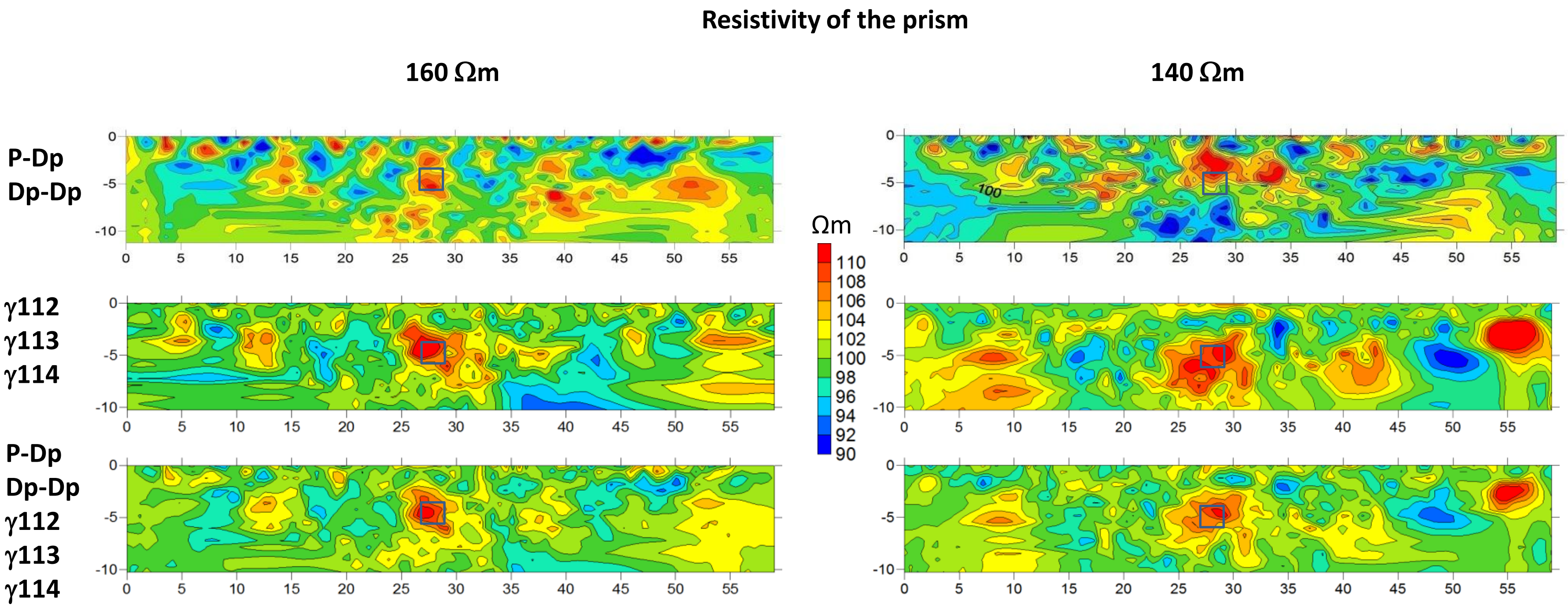
Resistivity of the prism
160 Ωm
140 Ωm
P-Dp
Dp-Dp
γ112
γ113
γ114
P-Dp
Dp-Dp
γ112
γ113
γ114
Ωm
110
108
106
104
102
100
98
96
94
92
90
100
0
-5
-10
0 5 10 15 20 25 30 35 40 45 50 55

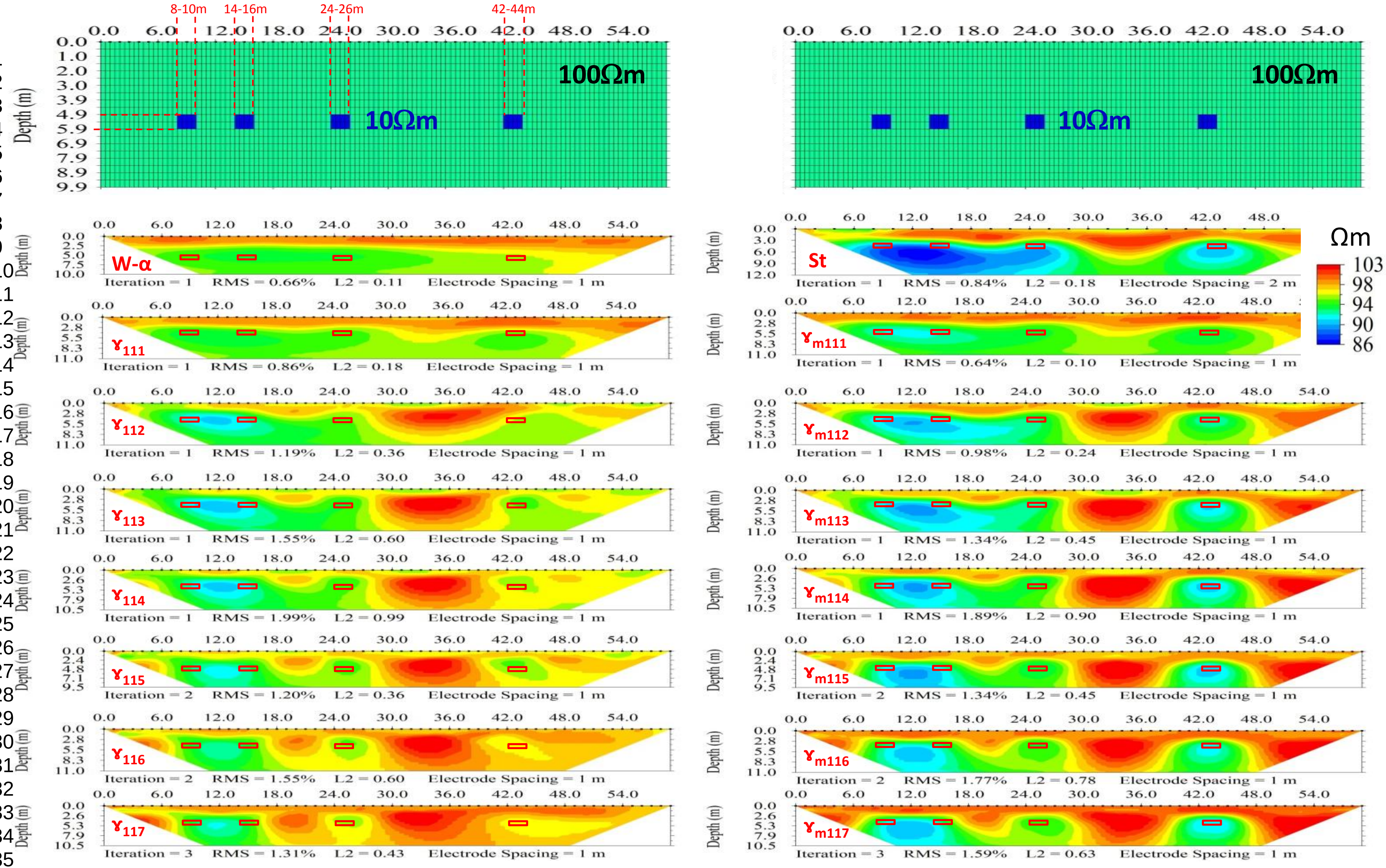
8-10m
14-16m
24-26m
42-44m
100Ωm
10Ωm
Depth (m)
W-α
St
Ωm
103
98
94
90
86
ϒ111
ϒ112
ϒ113
ϒ114
ϒ115
ϒ116
ϒ117
ϒm111
ϒm112
ϒm113
ϒm114
ϒm115
ϒm116
ϒm117
Iteration = 1 RMS = 0.66% L2 = 0.11 Electrode Spacing = 1 m
Iteration = 1 RMS = 0.84% L2 = 0.18 Electrode Spacing = 2 m
Iteration = 1 RMS = 0.86% L2 = 0.18 Electrode Spacing = 1 m
Iteration = 1 RMS = 0.64% L2 = 0.10 Electrode Spacing = 1 m
Iteration = 1 RMS = 1.19% L2 = 0.36 Electrode Spacing = 1 m
Iteration = 1 RMS = 0.98% L2 = 0.24 Electrode Spacing = 1 m
Iteration = 1 RMS = 1.55% L2 = 0.60 Electrode Spacing = 1 m
Iteration = 1 RMS = 1.34% L2 = 0.45 Electrode Spacing = 1 m
Iteration = 1 RMS = 1.99% L2 = 0.99 Electrode Spacing = 1 m
Iteration = 1 RMS = 1.89% L2 = 0.90 Electrode Spacing = 1 m
Iteration = 2 RMS = 1.20% L2 = 0.36 Electrode Spacing = 1 m
Iteration = 2 RMS = 1.34% L2 = 0.45 Electrode Spacing = 1 m
Iteration = 2 RMS = 1.55% L2 = 0.60 Electrode Spacing = 1 m
Iteration = 2 RMS = 1.77% L2 = 0.78 Electrode Spacing = 1 m
Iteration = 3 RMS = 1.31% L2 = 0.43 Electrode Spacing = 1 m
Iteration = 3 RMS = 1.59% L2 = 0.63 Electrode Spacing = 1 m

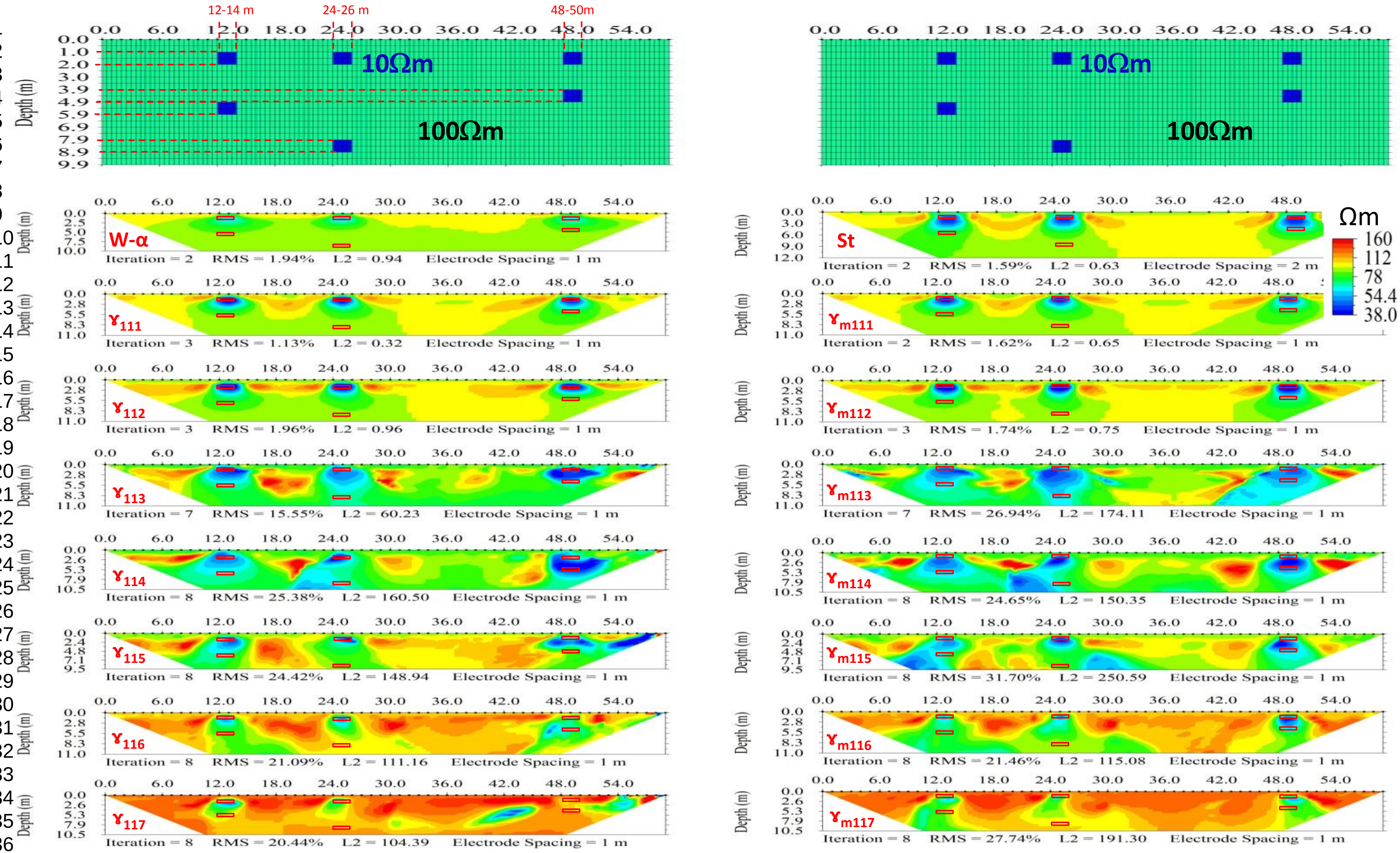

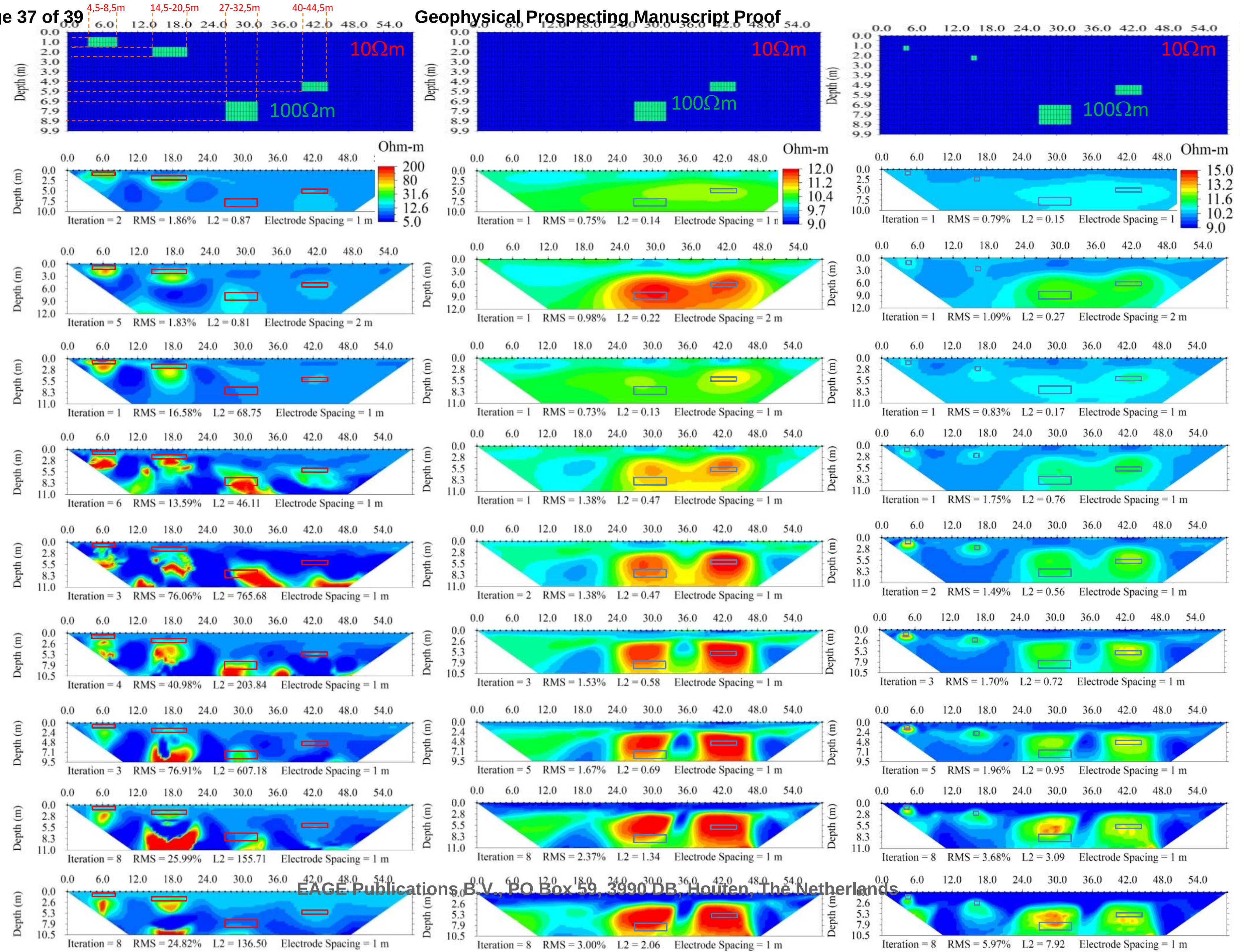
4,5-8,5m
14,5-20,5m
27-32,5m
40-44,5m
10Ωm
100Ωm
Depth (m)
Ohm-m
W-α
Iteration = 2 RMS = 1.86% L2 = 0.87 Electrode Spacing = 1 m
Iteration = 1 RMS = 0.75% L2 = 0.14 Electrode Spacing = 1 m
Iteration = 1 RMS = 0.79% L2 = 0.15 Electrode Spacing = 1
Iteration = 5 RMS = 1.83% L2 = 0.81 Electrode Spacing = 2 m
Iteration = 1 RMS = 0.98% L2 = 0.22 Electrode Spacing = 2 m
Iteration = 1 RMS = 1.09% L2 = 0.27 Electrode Spacing = 2 m
Iteration = 1 RMS = 16.58% L2 = 68.75 Electrode Spacing = 1 m
Iteration = 1 RMS = 0.73% L2 = 0.13 Electrode Spacing = 1 m
Iteration = 1 RMS = 0.83% L2 = 0.17 Electrode Spacing = 1 m
Iteration = 6 RMS = 13.59% L2 = 46.11 Electrode Spacing = 1 m
Iteration = 1 RMS = 1.38% L2 = 0.47 Electrode Spacing = 1 m
Iteration = 1 RMS = 1.75% L2 = 0.76 Electrode Spacing = 1 m
Iteration = 3 RMS = 76.06% L2 = 765.68 Electrode Spacing = 1 m
Iteration = 2 RMS = 1.38% L2 = 0.47 Electrode Spacing = 1 m
Iteration = 2 RMS = 1.49% L2 = 0.56 Electrode Spacing = 1 m
Iteration = 4 RMS = 40.98% L2 = 203.84 Electrode Spacing = 1 m
Iteration = 3 RMS = 1.53% L2 = 0.58 Electrode Spacing = 1 m
Iteration = 3 RMS = 1.70% L2 = 0.72 Electrode Spacing = 1 m
Iteration = 3 RMS = 76.91% L2 = 607.18 Electrode Spacing = 1 m
Iteration = 5 RMS = 1.67% L2 = 0.69 Electrode Spacing = 1 m
Iteration = 5 RMS = 1.96% L2 = 0.95 Electrode Spacing = 1 m
Iteration = 8 RMS = 25.99% L2 = 155.71 Electrode Spacing = 1 m
Iteration = 8 RMS = 2.37% L2 = 1.34 Electrode Spacing = 1 m
Iteration = 8 RMS = 3.68% L2 = 3.09 Electrode Spacing = 1 m
Iteration = 8 RMS = 24.82% L2 = 136.50 Electrode Spacing = 1 m
Iteration = 8 RMS = 3.00% L2 = 2.06 Electrode Spacing = 1 m
Iteration = 8 RMS = 5.97% L2 = 7.92 Electrode Spacing = 1 m

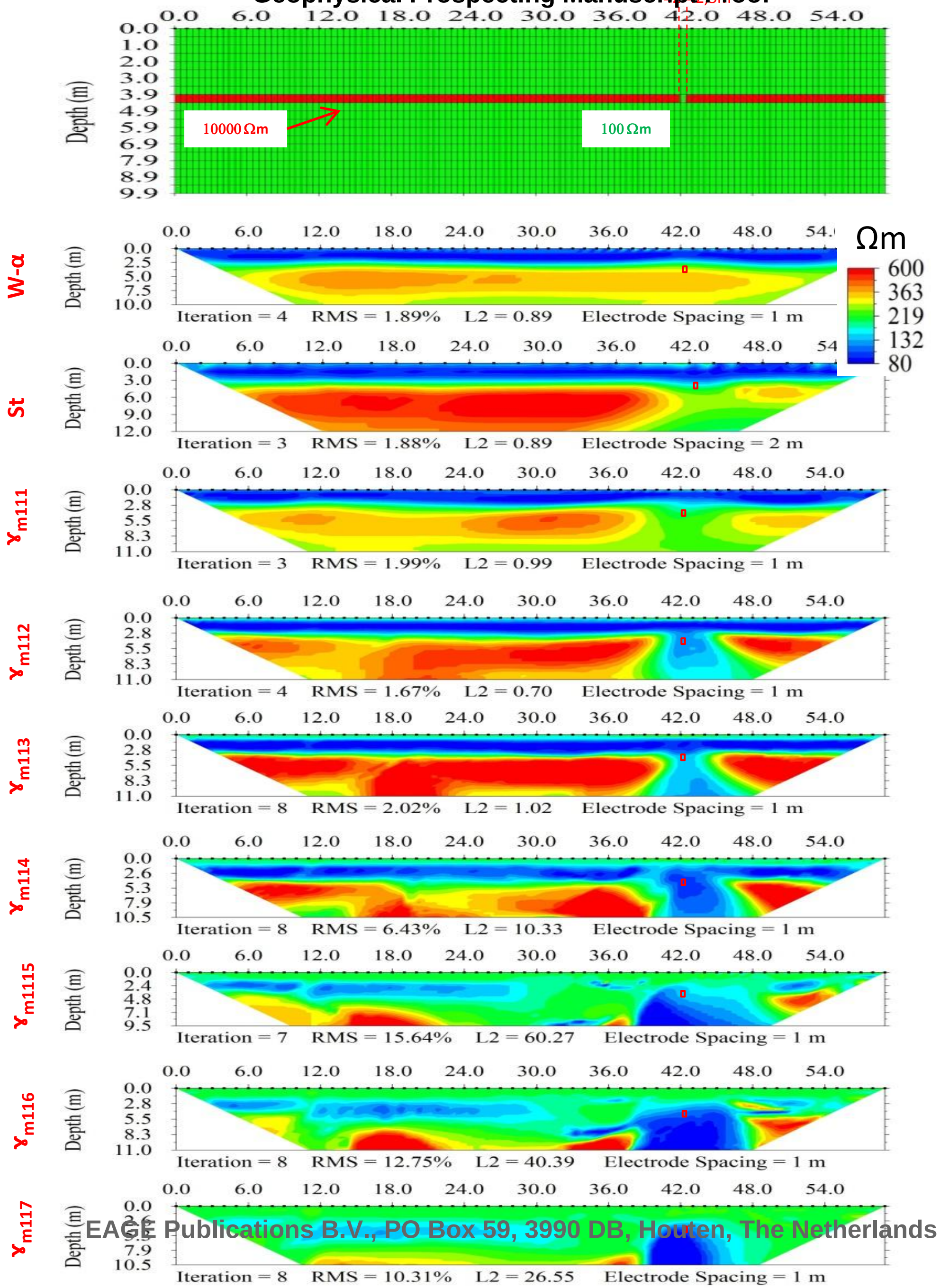
10000 Ωm
100 Ωm
Depth (m)
W-α
Iteration = 4 RMS = 1.89% L2 = 0.89 Electrode Spacing = 1 m
St
Iteration = 3 RMS = 1.88% L2 = 0.89 Electrode Spacing = 2 m
γm111
Iteration = 3 RMS = 1.99% L2 = 0.99 Electrode Spacing = 1 m
γm112
Iteration = 4 RMS = 1.67% L2 = 0.70 Electrode Spacing = 1 m
γm113
Iteration = 8 RMS = 2.02% L2 = 1.02 Electrode Spacing = 1 m
γm114
Iteration = 8 RMS = 6.43% L2 = 10.33 Electrode Spacing = 1 m
γm1115
Iteration = 7 RMS = 15.64% L2 = 60.27 Electrode Spacing = 1 m
γm116
Iteration = 8 RMS = 12.75% L2 = 40.39 Electrode Spacing = 1 m
γm117
Iteration = 8 RMS = 10.31% L2 = 26.55 Electrode Spacing = 1 m
Ωm
600
363
219
132
80

	Surface	Fig. 6.	Fig. 8-11.
Minimum apparent resistivity (Ωm) =	1	**-100000000**	**-10000**
Maximum apparent resistivity (Ωm) =	10000	**1000000**	10000
Keep All Data :	No	**Yes**	No
Lower-layer-thickness / Upper-layer-thickness =	1.1	**1**	**1**
Depth of Inverted Model / Depth of Pseudosection =	1.1	**1**	**1**
Max number of iteration of nonlinear inversion =	8	**20**	8
Stop RMS error =	3%	**5%**	**2%**
Stop when L2 norm is small enough:	No	**Yes**	No
Initial Lagrange multiplier or roughness factor =	10	**1**	**100**
Starting model:	Avg AppRes	**Pseudosection**	Avg AppRes
Estimated noise of resistivity data =	3%	**2%**	**2%**
Initial damping factor of resistivity =	10	**1**	**100**